Journal of Environmental Chemical Engineering 10 (2022) 108816

Contents lists available at ScienceDirect

Journal of Environmental Chemical Engineering

journal homepage: www.elsevier.com/locate/jece

Beneficial effects of nickel promoter on the efficiency of alumina-supported Co_3O_4 catalysts for lean methane oxidation

Andoni Choya, Beatriz de Rivas, Jose Ignacio Gutiérrez-Ortiz, Rubén López-Fonseca *

Chemical Technologies for Environmental Sustainability Group, Department of Chemical Engineering, Faculty of Science and Technology, University of the Basque Country UPV/EHU, Barrio Sarriena s/n, Leioa, Bizkaia, E-48940, Spain

ARTICLE INFO

Editor: Dong-Yeun Koh

Keywords:
Lean methane oxidation
Cobalt catalysts
Bimetallic Ni-Co catalysts
Nickel cobaltite
Vehicular natural gas
Oxygen mobility
Nickel promoter

ABSTRACT

In this work bimetallic Ni catalysts supported over Co-Al_2O_3 and monometallic Co-Al_2O_3 and Ni-Al_2O_3 catalysts were examined for the complete oxidation of methane. With a 30 % total metallic loading, the samples were synthesized by a sequential precipitation route. All samples were characterized by nitrogen physisorption, X-ray fluorescence, X-ray diffraction, Raman spectroscopy, scanning electron microscopy, scanning-transmission electron microscopy, X-Ray photoelectron spectroscopy, and temperature-programmed reduction with hydrogen and methane. Their catalytic performance was investigated in the temperature range of 200–600 °C with a space velocity of 60.000 h^{-1}. The bimetallic catalysts showed a better behavior in the oxidation reaction than the monometallic counterparts, mainly due to the good dispersion of Ni on the surface of the Co-Al_2O_3 samples. This has enabled the insertion of Ni^{2+} ions into the cobalt spinel lattice, which in turn provoked an increase in the amount of Co^{3+} species, and a subsequent enhanced mobility of oxygen species in the spinel. In this sense, the 5Ni/25Co catalyst showed the best performance, thus reducing the value of the T_{50} by 25 °C with respect to the monometallic catalysts.

1. Introduction

The efficient emission control of unburned methane in power plants and vehicles that use natural gas as a potential bridge fuel in the transition toward renewable energy is of vital importance [1,2], given that this pollutant is strongly involved in the greenhouse effect. Its potent greenhouse effect is around 25 times higher than that of CO_2. Presently, the most adequate approach to minimize the negative impact of the release of residual methane to the atmosphere is catalytic oxidation, which allows the direct conversion of the hydrocarbon to carbon dioxide and water. Probably there is no doubt that noble metal-based catalysts, particularly Pd catalysts, are the systems with the highest intrinsic oxidation power for this abatement strategy [3–7]. However, although large efforts are continuously being made to increase its thermal and chemical stability under operating conditions, its wide use is fundamentally penalized by economic reasons [8]. Thus, the proposal of cheaper, highly efficient, alternative catalysts is a challenge of relevant interest. Most studies have been focused on the use of transition metal oxides, namely nickel [9,10], manganese [11,12], copper [13] or iron [14]. However, it is widely accepted that spinel cobalt oxide (Co_3O_4) is the most attractive oxide phase for the lean methane catalytic combustion owing to the presence of variable valance states (Co^{3+}/Co^{2+}), its lower bonding energy of Co-O bonds and the high mobility of active oxygen species capable of activating the C-H bond [15–17]. Nevertheless, bulk cobalt oxide, as well as other bulk transition oxides, usually exhibit very poor textural and structural properties, especially when synthesized by simple methodology routes [18,19]. Thus, their good behavior is mainly assigned to their high metallic content (>70 %wt.), thereby resulting in a markedly low intrinsic activity. For this reason, several strategies have been proposed in order to enhance the performance of Co_3O_4-based catalysts with the ultimate goal of maximizing the population of active sites. The selection of the support for depositing the active phase is the first obvious approach to take into consideration. Furthermore, advances in the optimized design of supported catalysts are highly relevant since the final configuration of a commercial catalytic unit will be a structured catalyst operating with large gas flows [20]. These catalysts will be surely prepared by washcoating a thin catalytic layer (metal oxide/support) onto the surface a monolithic/foam substrate.

In this sense, it must be stated that, owing to the high affinity of cobalt for most typical inorganic supports (γ-Al_2O_3, SiO_2 or MgO), a certain fixation of cobalt as less active $CoAl_2O_4$, $CoSiO_3$ or Co-Mg mixed

* Corresponding author.
E-mail address: ruben.lopez@ehu.eus (R. López-Fonseca).

https://doi.org/10.1016/j.jece.2022.108816
Received 26 July 2022; Received in revised form 30 September 2022; Accepted 17 October 2022
Available online 26 October 2022
2213-3437/© 2022 The Author(s). Published by Elsevier Ltd. This is an open access article under the CC BY-NC-ND license (http://creativecommons.org/licenses/by-nc-nd/4.0/).

oxides must be assumed [21,22]. This unavoidably involves the use of relatively high Co loadings (20–40 %wt.) to compensate partially the useless presence of a fraction of deposited Co. The use of alternative supports such ceria or alpha-alumina prevented this strong undesired interaction but their relatively low intrinsic surface area do not usually lead to a substantially improvement in behavior of the resultant composite catalysts [23,24]. A complementary option to adjust the amount and/or reactivity of oxygen species is the addition of a promoter that could improve the reducibility of the resultant catalyst at low temperatures. Based on its comparable ionic radius and coordination and oxidation states to cobalt, nickel is the most preferred promoter. The incorporation of nickel is mainly justified by the notable activity shown by the $NiCo_2O_4$ spinel that can be formed from the interaction between cobalt and nickel. This approach is quite interesting for methane oxidative abatement [25–28], but requires a large amount of nickel (around 50 % of the Co content for a Ni/Co molar ratio of 0.5). In addition, the synthesis of stoichiometric nickel cobaltite is largely dependent on very well controlled synthesis conditions in terms of calcination temperature and selected preparation route, usually oriented to the synthesis of the mixed oxide in its bulk form. In other words, it would be of interest to explore alternatives for taking advantage of the known beneficial effects of nickel promoter, without the need of large amounts of this additive and using a relatively simple route for obtaining an active Ni-promoted cobalt catalyst.

Therefore, the objective of this work is the study of Ni/Co-Al_2O_3 catalysts for the oxidation of methane under conditions similar to those found in the exhaust of vehicular natural gas engines (relatively low residence times, and presence of water and carbon dioxide). Thus, for a total metal loading of 30 % by weight, the effect of the addition of 5 % and 10 %wt.Ni on cobalt catalysts with a content of 25 % and 20 %wt. Co, respectively, was investigated. These samples were prepared by sequential precipitation of cobalt and nickel, with an intermediate calcination step. Along with these catalysts, monometallic cobalt (20 %, 25 % and 30 %wt.) and nickel (30 %wt.) catalysts with a content of 30 % wt. (30Co and 30Ni, respectively) were synthesized as well for comparative purposes.

2. Materials and methods

2.1. Synthesis of the catalysts

All oxide catalysts were synthesized following a precipitation route over a thermally-stabilized (calcined at 850 C for 8 h) γ-Al_2O_3 (Saint Gobain), which selected as the support. Three cobalt oxide catalysts, namely 20Co, 25Co and 30Co samples, were prepared by precipitation of aqueous solution of cobalt nitrate hexahydrate with an adjusted concentration to obtain the desired nominal Co loading (20, 25 and 30 wt. %, respectively), at 80 °C using an aqueous solution of sodium carbonate (1.2 M) until reaching a pH of 8.5. After precipitation, the precursors were dried at 110 °C overnight.

Then, the catalyst precursors were calcined at 600 C for 8 h in static air. In the case of the reference nickel catalyst (30Ni, with a nominal Ni content of 30 %wt.), the starting salt was nickel nitrate hexahydrate. This sample was also submitted to the same aforementioned thermal treatment.

Two bimetallic Ni-Co catalysts were obtained by sequential precipitation using the same metallic salts and precipitating conditions (pH = 8.5, 80 ºC). Thus, nickel was added to the previously prepared 20Co and 25Co samples with a nominal content of 10 % and 5 %wt., respectively. Thus, the total metallic loading of these samples was fixed at 30 %wt. Finally, the samples were again calcined at 600 C for additional 4 h. In this way, both monometallic and bimetallic catalysts were activated under identical thermal conditions. The resulting Ni-Co catalysts were designated as 10Ni/20Co and 5Ni/25Co.

2.2. Characterization techniques

The supported catalysts were characterized by a wide number of analytical techniques, including scanning electron microscopy (SEM) coupled to energy dispersive X-ray spectroscopy (EDX), scanning transmission electron microscopy - high angle annular dark field (STEM-HAADF) coupled to EDX mapping, wavelength dispersive X-ray fluorescence (WDXRF), N_2 physisorption, X-Ray diffraction (XRD), Raman spectroscopy, X-Ray photoelectron spectroscopy (XPS), temperature-programmed reduction with hydrogen (H_2-TPR) and temperature programmed reaction with methane (CH_4-TPRe). Experimental details on each of these techniques are included in the Supplementary Material.

The activity of the synthesized catalysts for the oxidation of residual methane was determined in a fixed bed reactor (Microactivity by PID Eng&Tech S.L.) between 200 and 600 °C. The reaction products were quantified with an on-line gas chromatograph (Agilent Technologies 7890 N) equipped with a thermal conductivity detector. In each reaction test one gram of catalyst (particle size 0.25–0.30 mm) diluted with 1 g of inert quartz (particle size 0.5–0.8 mm) was used. A reaction mixture of composition 1 %CH_4/10 %O_2/89 %N_2 was used with a total flow rate of 500 mL min^{-1}, which represents an approximate space velocity of 60,000 h^{-1}. To ensure that the mass and heat transfer effects were not affecting the kinetic results, the inter- and intraphase concentration and temperature gradients (Table S1, Supplementary Material) were verify to be negligible according to the criteria proposed by Eurokin [29]. The absence of mass and heat transfer limitations within the reactor was evaluated not only under differential conditions (X < 20 %) but also under the least favorable conditions (450–600 ºC). Additionally, the stability of the most promising catalyst with time on stream was evaluated at constant temperature (575 °C) for a total reaction interval of 150 h under alternate dry, humid (10 %) or CO_2-rich (10 %) conditions while maintaining the O_2/CH_4 molar ratio at 10.

3. Results and discussion

3.1. Characterization of the catalysts

Prior to the discussion of the characterization results of the prepared catalysts, it is highly relevant to remark that the variety of oxide phases that can be present in Co- and/or Ni-containing gamma-alumina supported catalysts thermally activated at moderate temperatures (600 °C) is wide. In addition to the expected Co_3O_4 and NiO oxides, and obviously the γ-Al_2O_3 support, the presence of mixed spinels such as $CoAl_2O_4$ and $NiAl_2O_4$ is normally unavoidable. These new metallic oxides are formed due to the strong interaction between the Co and Ni species and the support that results in the partial insertion of Co or Ni atoms into the lattice of the gamma alumina. Moreover, it is commonly accepted that the morphology of these spinels will be essentially amorphous since its transformation into a crystalline structure requires calcination temperatures as high as 800–850 °C [30,31]. Besides, the formation of Ni/Co mixed oxides can occur. Thus, based on these considerations both monometallic (20Co, 25Co, 30Co and 30Ni) and bimetallic (5Ni/25Co and 10Ni/20Co) catalysts were thoroughly investigated by a wide number of analytical techniques including N_2-physisorption, SEM coupled to EDX, XRF, STEM-HAADF coupled to EELS or EDX, Raman spectroscopy, XPS, H_2-TPR and CH_4-TPRe.

Table 1 include the textural properties of the metal oxide catalysts. The corresponding pore size distribution are included in Fig. S1, Supplementary Material. The thermally-stabilized (calcined at 850 °C for 8 h) blank alumina support showed a surface area of around 140 m^2 g^{-1} and a pore volume of 0.56 cm^3 g^{-1}. Its pore size distribution was bimodal with maxima located at 110 and 150 Å. After the addition of increasing amounts of cobalt (20Co, 25Co and 30Co samples), the surface area appreciably decreased to 120–108 m^2 g^{-1} due to pore blocking. Accordingly, their pore volume was notably affected since it decreased to 0.35–0.29 cm^3 g^{-1}. The resultant narrower average pore

Table 1
Textural and structural properties of the synthesized catalysts.

Sample	Surface area, $m^2\ g^{-1}$[a]	Pore volume, $cm^3\ g^{-1}$[a]	Average pore size, Å	Co_3O_4 crystallite size, nm
Al_2O_3	139	0.56	110, 150	–
30Co	108	0.29	109	35
25Co	118	0.34	94	19
5Ni/25Co	109	0.33	107	19
20Co	120	0.35	98	21
10Ni/20Co	112	0.36	107	17
30Ni	128	0.37	95	14[a]

[a] NiO crystallite size.

size was in the 94–98 Å range. It was then evident that cobalt species preferentially deposited on the larger pores of the support (150 Å). In the case of the nickel catalyst (30Ni sample), the addition of the metal affected the textural properties to lesser extent when compared with its cobalt counterpart with the same loading (30Co sample). Thus, a surface area close to 130 $m^2\ g^{-1}$ was observed. This was probably connected to a trade-off effect between the pore blocking of the support by nickel and the newly formed $NiAl_2O_4$ phase with a high intrinsic surface area. This rationale was supported by the notable surface area (170 $m^2\ g^{-1}$) of an as-prepared bulk $NiAl_2O_4$, which was prepared by precipitation and calcined at 600 °C.

Regarding the bimetallic catalysts, the addition of nickel (5–10 % wt.) to the Co/Al_2O_3 samples produced a loss of specific surface area0 around 7–8 % with respect to the corresponding monometallic sample with the same Co content (25Co and 20Co samples). Furthermore, while the pore volume remained almost constant, a slight increase in the mean pore size (from 94 to 98–107 Å) was found. In view of these results, it could be concluded that the deposition of the promoter had no marked effect on the textural properties, as relatively similar surface areas, pore volumes, and pore diameters were obtained independently from the Ni/Co ratio of the bimetallic samples.

The microstructural morphology of the four monometallic samples (20Co, 25Co, 30Co and 30Ni) and the two bimetallic samples (5Ni/25Co and 10Ni/20Co) was examined by SEM. Irrespective of the composition of the catalysts, the micrographs (Fig. S2, Supplementary Material) revealed a heterogeneous surface on which irregular particles with sizes ranging from 5 to 20 μm are arranged with an aggregated morphology. Elemental identification and quantitative compositional information could be obtained by an energy dispersive X-Ray analyzer. Thus, the average surface composition of various defined regions (40 ×40 μm with a sampling depth of about 1 μm) for each catalyst was determined. Table 2 compares the bulk and surface composition as analyzed by XRF and EDX. As for the monometallic samples, an expected surface enrichment was found as revealed by their comparatively higher metal (Co or Ni)/Al molar ratios in relation to the respective bulk molar ratios. Particularly, this ratio at the surface as determined by EDX increased by a factor of 1.6–2.1 in the case of the Co-containing catalysts, and a factor of 1.1 in the case of the 30Ni sample.

The monometallic 30Co and 30 Ni samples were also examined by scanning transmission electron microscopy–high-angle annular dark field (STEM–HAADF). Additionally, EELS elemental maps (Fig. S3, Supplementary Material) were obtained for certain regions in each sample to examine the spatial distribution of these metals in the catalysts. It was revealed that both Co and Ni were homogeneously distributed over the surface and no large uncoated support regions were apparently observed. This suggested a relative good metallic coverage of the alumina surface. The samples were characterized by the presence of polycrystallites (in some cases formed by the apparent attachment of smaller crystallites) with sizes ranging from 10 to 40 nm. It is worth pointing out the detection of crystalline phases on the surface of the 30Ni catalyst was comparatively less frequent, thereby suggesting the deposited metallic species on this sample exhibited a more amorphous nature.

As for the bimetallic Ni-Co catalysts, it must be pointed that, although the Ni/Co molar ratio at the surface was higher than the corresponding bulk ratio, this increase was not very marked, from 0.23 to 0.25 over the 5Ni/25Co sample and from 0.58 to 0.60 over the 10Ni/20Co sample. This suggested a partial Ni diffusion into the cobalt catalytic layer. Likewise, surface chemical mapping, in this case carried out by STEM-HAADF coupled to EDX, was carried out to study the distribution of both metals on the surface of the bimetallic catalysts. As seen in the compositional maps included in Figs. 1 and 2, both cobalt and nickel were relatively well dispersed over the surface, with no visible clustering or agglomeration of either metal. Seemingly, the mixing between cobalt and nickel seemed to be equally intimate for both Ni-Co catalysts.

X-ray diffraction analysis was used to identify the crystalline phases present in each oxide catalyst. The corresponding patterns are included in Fig. 3. The monometallic cobalt catalysts (20Co, 25Co and 30Co) showed the characteristic signals of a cubic spinelic phase (2θ = 19.2, 31.4, 37.1, 45.1, 59.6 and 65.5°) that would be in agreement with the formation of Co_3O_4 (ICDD 00–042–1467) and/or $CoAl_2O_4$ (ICDD 00–044–0160). Certainly, as will be evidenced later by both Raman spectroscopy and H_2-TPR analysis, these samples consisted of a mixture of these cobalt oxides. However, while assuming the present cobalt aluminate will be preferentially amorphous under mild calcination at 600 °C, the visible diffraction signals in these patterns could be exclusively assigned to highly crystalline Co_3O_4. On the other hand, the reference 30Ni catalyst evidenced the typical signals of a cubic phase at 2θ = 37.2; 43.1; 62.9 and 75.4° corresponding to the presence of nickel oxide NiO (ICDD 00–089–7131). It must pointed out that although the formation of nickel aluminate is highly likely, this could not be detected probably due to its poor crystallinity. Recall that no clear signals attributable to crystalline $NiAl_2O_4$ (ICDD 00–078–1601) were observed. However, and similar to the results found for the Co catalysts, the existence of this spinel will be verified by redox and structural studies. Finally, a weak signal attributable to γ-alumina (ICDD 01–074–2206) support was also observed at 2θ = 67.2° over these four monometallic samples. The diffractograms of the bimetallic Ni-Co catalysts did not reveal the presence of segregated NiO, which suggested that this oxide was finely dispersed on the Co/Al_2O_3 matrix. Thus, only diffraction signals related to Co_3O_4 were noted. The crystallite size of this oxide (Table 1) was determined from the full width half maximum of the characteristic signal at 37.1°, using the Bragg equation. It thus ranged

Table 2
Bulk (XRF) and surface (EDX) composition of the synthesized catalysts.

XRF						SEM-EDX				
Sample	Co %wt.	Ni %wt.	Co/Al	Ni/Al	Ni/Co	Co %wt.	Ni %wt.	Co/Al	Ni/Al	Ni/Co
30Co	27.0	–	0.37	–	–	30.7	–	0.57	–	–
25Co	23.2	–	0.29	–	–	29.2	–	0.52	–	–
5Ni/25Co	21.9	5.1	0.30	0.07	0.23	28.2	6.2	0.60	0.23	0.25
20Co	18.6	–	0.22	–	–	28.5	–	0.47	–	–
10Ni/20Co	17.3	10.0	0.24	0.14	0.58	27.1	13.0	0.76	0.33	0.60
30Ni	–	27.1	–	0.36	–	–	30.9	–	0.41	–

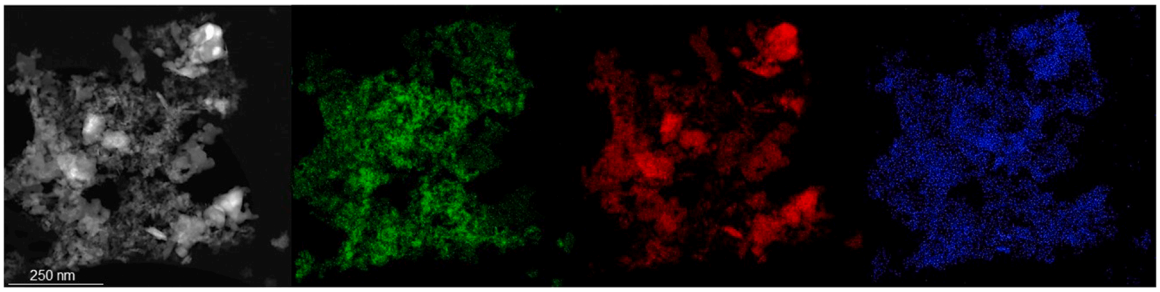

Fig. 1. STEM-HAADF/EDX elemental maps of the 5Ni/25Co catalyst. Aluminum (green), cobalt (red) and nickel (blue).

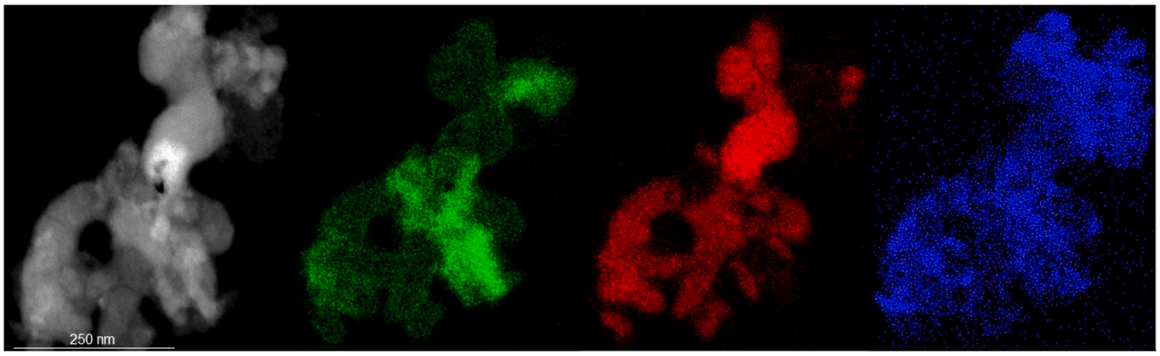

Fig. 2. STEM-HAADF/EDX elemental maps of the 10Ni/20Co catalyst. Aluminum (green), cobalt (red) and nickel (blue).

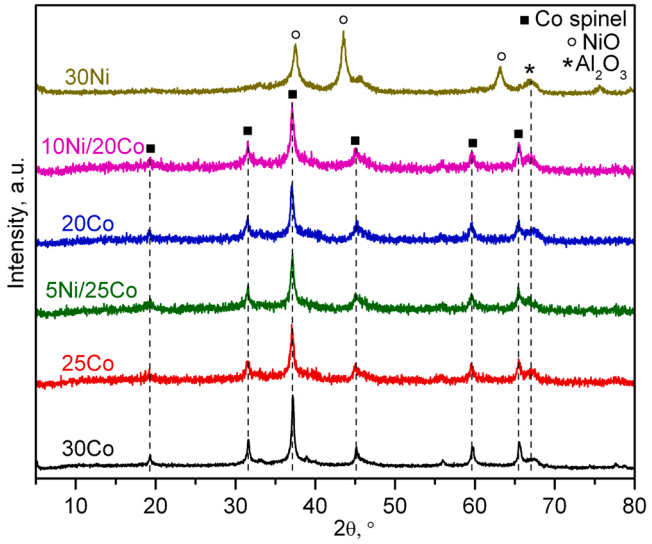

Fig. 3. X-ray diffractograms of the synthesized catalysts.

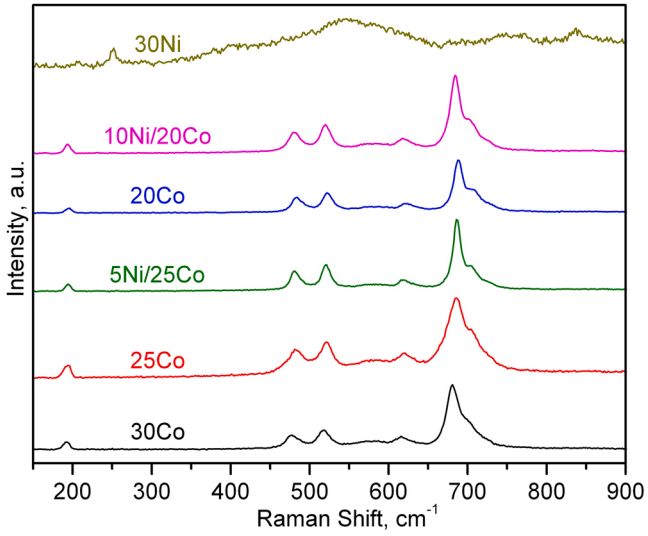

Fig. 4. Raman spectra of the synthesized catalysts.

from 19 to 21 nm for the 20Co and 25Co samples to 35 nm for the 30Co catalyst. Interestingly, the addition of nickel to the Co/Al_2O_3 samples did not significantly alter the crystallite size (17–19 nm). On the other hand, the crystallite size of the NiO phase in the 30Ni catalyst was 14 nm.

The examination of the structure of the oxide catalysts was carried out by Raman spectroscopy (Fig. 4). The Raman spectra of the 20Co, 25Co and 30Co samples displayed the five typical vibration modes of Co_3O_4 at 196, 480, 520, 619 and 687 cm^{-1} [32]. The presence of $CoAl_2O_4$ was also evidenced by the two shoulders located at 706 and 725 cm^{-1} [33]. Apparently the contribution of these two additional signals was more marked in the case of the 20Co and 25Co, thus suggesting that the formation of cobalt aluminate would be favored with lower loadings of cobalt. Therefore, the cobalt phases present in the studied Co/Al_2O_3 catalysts would be a mixture of Co_3O_4 and $CoAl_2O_4$, with a higher relative abundance of the aluminate phase when the total Co content of the sample was lower. Lastly, the Raman spectra of the 30Ni catalyst was dominated by a wide signal located at 545 cm^{-1}, which would be coherent with the presence of a mixture of NiO (its main Raman mode is located at 510 cm^{-1}) and $NiAl_2O_4$ (its main Raman mode is located at 574 cm^{-1}). The existence of the nickel spinel was further evidenced by the weaker signals at 746 cm^{-1} and 835 cm^{-1} [34]. On the other hand, the addition of nickel to the Co-Al_2O_3 catalysts did not substantially modify the spectra of the resulting samples (5Ni/25Co and 10Ni/20Co). Thus, the only observable Raman modes coincided with those corresponding to the parent cobalt catalyst, namely a mixed contribution of Co_3O_4 and $CoAl_2O_4$ phases. The marked

presence of NiO and/or $NiAl_2O_4$ could be ruled out in these bimetallic catalysts.

The surface composition of the samples and, more importantly, the distribution of the various metallic (cobalt and nickel) and oxygen species was investigated by analyzing the $Co2p_{3/2}$ (777–792 eV), $Ni2p_{3/2}$ (850–870 eV) and O1s (526–538 eV) XPS spectra of the samples, as shown in Fig. 5. Prior to the analysis in the XPS chamber, the as-calcined oxide catalysts were stored in airtight polyethylene containers in order to limit their exposure to ambient air. The $Co2p_{3/2}$ spectra were deconvoluted into three main and two satellite contributions. The main contributions were located at 779.5, 780.7 and 782.4 eV, and were tentatively attributed to the presence of Co^{3+}(Co_3O_4), Co^{2+}(Co_3O_4 and/or $CoAl_2O_4$) and Co^{2+}(CoO) species, respectively [35]. For all oxide catalysts, the relative abundance of the signal related to CoO was lower than 10 % of the total $Co2p_{3/2}$ signal. This species was assumed to be formed by reduction under the vacuum conditions in the XPS chamber. The two signals located at 785.5 and 789.5 eV were assigned to the shake-up satellite peaks from Co^{2+} and Co^{3+} ions.

Following a similar procedure, the $Ni2p_{3/2}$ spectra were deconvoluted into five signals. The three main signals were centered at around 853.9, 855.4 and 856.9 eV and were associated with the presence of Ni^{2+}(NiO), Ni^{2+}(nickel belonging to a spinelic phase) and Ni^{3+}(Ni_2O_3) species, respectively [36]. The satellite contribution of the spectra was dominated by an intense signal located at 861.0 eV, characteristic of the presence of Ni^{2+}, and a small shoulder at 865.3 eV, which was a consequence of the relatively reduced presence of Ni^{3+} ions in these samples. Finally, the O1s spectra of the samples was characterized by three signals located at 529.3, 531.3 and 532.6 eV, which were attributed to oxygen species from the crystalline lattice (O_{latt}), superficially adsorbed oxygen species (O_{ads}), and carbonate and hydroxyl species, respectively [37]. From the quantification of the aforementioned spectra, the elemental surface composition and the distribution of ionic species could be determined, as summarized in Table 2.

As for the monometallic cobalt catalysts, it was observed that the Co^{3+}/Co^{2+} molar ratio was in the 0.60–0.69 range, which was markedly lower than that expected for the exclusive presence of Co_3O_4. These moderate ratios suggested the presence of Co^{2+}-rich oxides such as $CoAl_2O_4$, as previously pointed out by Raman spectroscopy. In fact, it could be inferred that cobalt aluminate was preferentially formed for low Co loadings, since the 20Co sample showed the lowest Co^{3+}/Co^{2+} ratio (0.60). On the other hand, the $Ni2p_{3/2}$ spectrum of the pure nickel catalyst (30Ni) clearly evidenced the presence of comparable amounts of nickel oxide and nickel aluminate. Hence, in addition to traces of Ni^{3+} species, the observed nickel was in the form of NiO (36 %) and Ni_2AlO_4 (49 %). The incorporation of nickel markedly affected the distribution of cobalt species on the 5Ni/25Co and 10Ni/20Co catalysts. Interestingly, the addition of this promoter favored the presence of Co^{3+} cations. This enrichment was a priori related to the partial insertion of Ni^{2+} ions into the structure of the Co_3O_4, which would imply the generation of the mixed $NiCo_2O_4$ spinel to some extent. In this sense, since the increased population of Co^{3+} ions was more noticeable for the 5Ni/25Co catalyst (with a Co^{3+}/Co^{2+} molar ratio of 0.80) in comparison with the 10Ni/20Co sample (with a Co^{3+}/Co^{2+} molar ratio of 0.64), a more extensive formation of nickel cobaltite was likely for low concentrations of the promoter. Accordingly, these samples showed a high population of Ni^{2+} species related a spinel-like phase ($NiCo_2O_4$) at the cost of Ni^{2+} as NiO. On the other hand, the presence at the surface of Ni^{3+} species (as Ni_2O_3) was also observed over the bimetallic Ni-Co and 30Ni samples, which was favored for low Ni loadings. Finally, it must be remarked that all these structural changes induced by nickel addition on the surface of the alumina supported cobalt catalysts led to an increase of lattice oxygen species. These are widely accepted to play a key role in methane oxidation [38]. Hence, the O_{latt}/O_{ads} molar ratios were between 0.50 (10Ni/20Co) and 0.63 (5Ni/25Co), apparently higher than those of the respective Ni-free counterparts (0.25 for 20Co and 0.43 for 25Co).

The analysis of the metallic catalysts by temperature-programmed reduction with hydrogen (H_2-TPR) could be also helpful in identifying the nature of the oxide species present in each sample. The corresponding profiles are compared in Fig. 6. The redox behavior of the monometallic catalysts (20Co, 25Co, 30Co and 30Ni) was initially discussed in order to facilitate the subsequent interpretation of the results corresponding to the bimetallic Ni-Co samples. As for the Co-containing

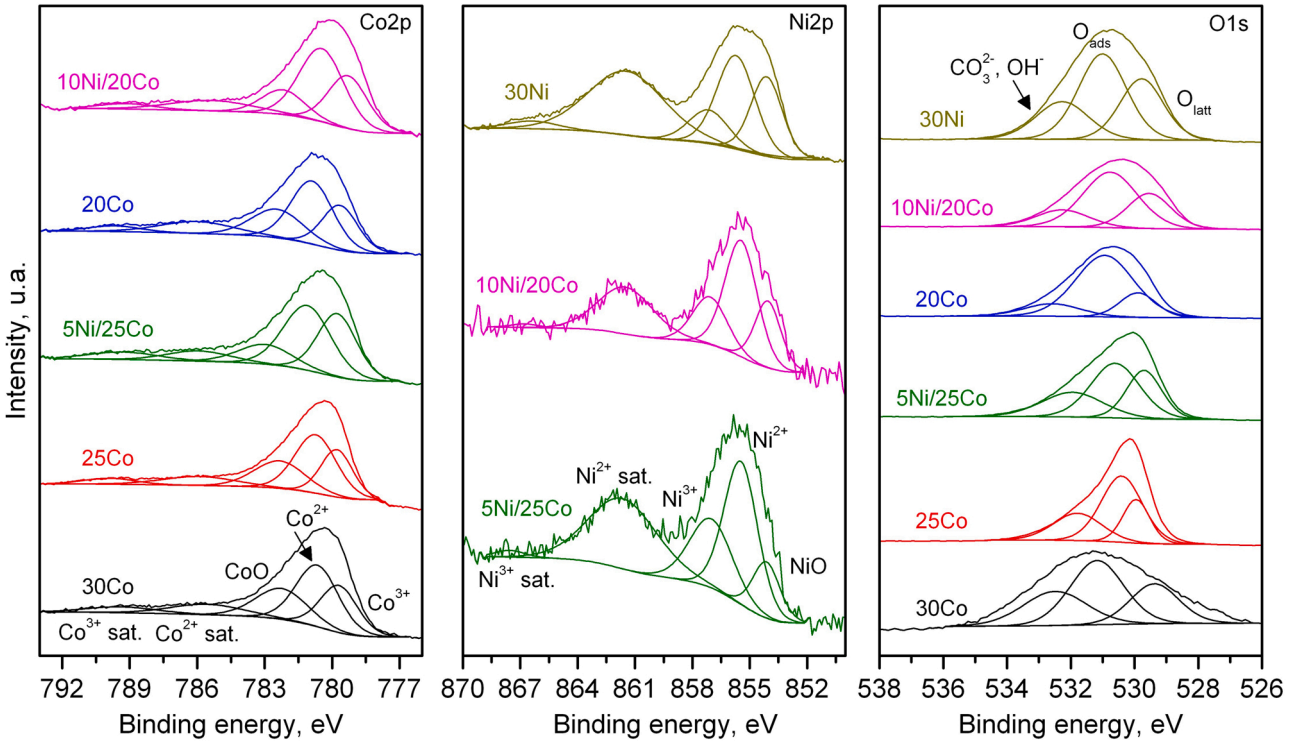

Fig. 5. Co2p, Ni2p and O1s XPS spectra of the synthesized catalysts.

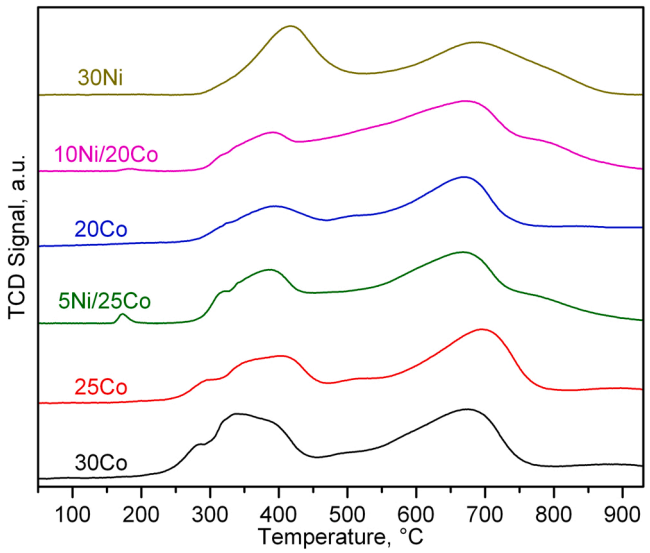

Fig. 6. H_2-TPR profiles of the synthesized catalysts.

catalysts, two reduction events were clearly observable. Above 800 °C no measurable H_2 consumption was noticed. Thus, the low-temperature uptake at 250–500 °C was assigned to the reduction of free Co_3O_4, according to the two-stage $Co^{3+} \rightarrow Co^{2+} \rightarrow Co^0$ process [39]. The stoichiometric H_2:Co molar ratio of this step is 1.33. The high-temperature consumption in the 550–750 °C corresponded to the reduction of the present cobalt aluminate [40]. The H_2:Co stoichiometry for full reduction of this oxide is 1. Note that the presence of this highly stable oxide was in agreement with the results derived from both Raman and XPS spectroscopies. Table 3 includes the total H_2 uptake of each monometallic sample, which increased from 3.5 to 5.2 mmol H_2 g^{-1}. The comparison of these values with the theoretical consumption expected when assuming that all cobalt was exclusively present as Co_3O_4 (which would vary from 4.2 to 6.1 mmol H_2 g^{-1}) resulted in reducibility degrees around 84–85 %. From these values, the relative distribution of Co atoms as Co_3O_4 or $CoAl_2O_4$ could be estimated. Hence, the abundance of cobalt as cobalt oxide gradually increased with the Co loading from 35 % to 37 % and 39 % over the 20Co, 25Co and 30Co samples, respectively.

On the other hand, the fixation of the deposited metal as aluminate due to the strong metal-support interaction was observed for the 30Ni nickel catalyst as well. Therefore, its reduction trace also revealed two distinct H_2 uptakes at moderate (400 °C) and high (700 °C) temperatures, which were associated with the presence of NiO and $NiAl_2O_4$, respectively [41], in consonance with the Raman and XPS results. It is worth pointing out that the stability of nickel aluminate was significantly higher than that of cobalt aluminate since its full reduction needed temperatures higher than 800 °C. Both oxides present a H_2:Ni stoichiometry of 1. A relative good agreement was found between the experimental (4.5 mmol H_2 g^{-1}) and theoretical (4.6 mmol H_2 g^{-1}) consumptions. Consequently, a reducibility close to 100 % was evidenced. An estimation of the relative contribution of each nickel species suggested a roughly similar population of both oxide phases (43 %Ni as NiO and 57 %Ni as $NiAl_2O_4$).

The incorporation of nickel to the 20Co and 25Co samples did not significantly altered the shape of the corresponding redox patterns since these also showed two reduction uptakes at low (250–475 °C) and high temperatures (550–750 °C). In view of the reduction pattern of the 30Ni sample, it was reasonable to expect that the reduction of the Ni^{2+} species present in the bimetallic samples (preferentially as free NiO) would occur mainly at the low temperature window, thus simultaneously coinciding with the reduction of Co_3O_4 species. Likewise, a small uptake at around 170 °C, which was not observed in the monometallic Co-Al_2O_3 counterparts, was visible. This consumption was assigned to the reduction of finely dispersed NiO nickel species [42,43], and was comparatively more noticeable for the 5Ni/25Co catalyst. In addition, the Ni-Co samples exhibited an appreciable shoulder at around 800 °C that was related to the reduction of nickel aluminate, probably due the strong interaction of added nickel with trace amounts of uncovered alumina.

As shown in Table 3, owing to their higher total metallic loading the quantitative analysis of the reduction profiles expectedly evidenced a higher H_2 uptake for the bimetallic samples (5Ni/25Co and 10Ni/20Co) in comparison with the respective Ni-free cobalt counterparts (25Co and 20Co, respectively). Thus, the overall reducibility increased from 4.4 to 5.2 mmol H_2 g^{-1} in the case of 25Co and 5Ni/25Co catalysts, and from 3.5 to 5.2 mmol H_2 g^{-1} in the case of the 20Co and 10Ni/20Co catalysts. Note that the total uptake of the Ni/Co samples (5.2 mmol H_2 g^{-1}) was virtually identical to that of the 30Co catalyst (5.2 mmol H_2 g^{-1}). Also relevant was the fact the reducibility, within the experimental error, of the bimetallic samples was promoted after the addition of nickel. Thus, it increased from 84 % over the 25Co sample to 90 % over the 5Ni/25Co sample, and from 84 % over the 20Co sample to 92 % over the 10Ni/20Co sample. This suggested that the incorporation of nickel promoted the presence of Co^{3+} cations with a higher H_2 consumption per Co (1.5). As revealed by XPS, the simultaneous presence of nickel and cobalt could result in the formation of $NiCo_2O_4$-like spinel that ultimately increased the catalyst overall reducibility. Moreover, keeping in mind that the catalytic activity in the methane oxidation is expected to be mainly controlled by oxygen species consumed in the low-temperature range, it was found that the introduction of nickel was efficient for achieving this purpose. Hence, this uptake increased from 1.2 (20Co) to 1.6 mmol H_2 g^{-1} (10Ni/20Co), and from 1.7 (25Co) to 2.0 mmol H_2 g^{-1} (5Ni/25Co). In this latter case, a comparable uptake was found with respect to the 30Co catalyst.

The reactivity of the available oxygen species present in the synthesized catalysts was complementary investigated by monitoring the conversion of methane in the absence of oxygen at increasing temperature (CH_4-TPRe). The explored temperature range was 50–600 °C with a heating ramp of 10 °C min^{-1}. The samples were then kept at 600 °C for 15 min. The composition of the product stream was followed by mass spectrometry ($m/z = 44$ (CO_2), 28 (CO) and 2 (H_2) signals). The resulting profiles of the bimetallic Ni-Co and monometallic (30Co and 30Ni) catalysts are shown in Fig. 7. Theoretically, methane is expected to be oxidized to carbon oxides at relatively low temperatures by active oxygen species at the catalyst surface. This will result in a progressive reduction of the metallic oxides, and a concomitant high-temperature conversion of methane into reforming products including CO, H_2 and CO_2, and/or cracking products (H_2 and carbonaceous deposits) that will

Table 3
Surface composition of the synthesized catalysts as determined by XPS.

Sample	Co %wt.	Ni %wt.	Co/Al	Ni/Al	Ni/Co	Co^{3+}/Co^{2+}	O_{latt}/O_{ads}	Ni^{3+}/Ni	NiO/Ni	Ni^{2+}/Ni
30Co	30.8	–	0.58	–	–	0.69	0.52	–	–	–
25Co	27.9	–	0.48	–	–	0.63	0.43	–	–	–
5Ni/25Co	29.8	6.1	0.71	0.15	0.21	0.80	0.63	0.32	0.16	0.52
20Co	25.1	–	0.39	–	–	0.60	0.25	–	–	–
10Ni/20Co	25.7	10.3	0.50	0.20	0.40	0.64	0.50	0.23	0.24	0.53
30Ni	–	–	–	0.84	–	–	0.65	0.16	0.36	0.49

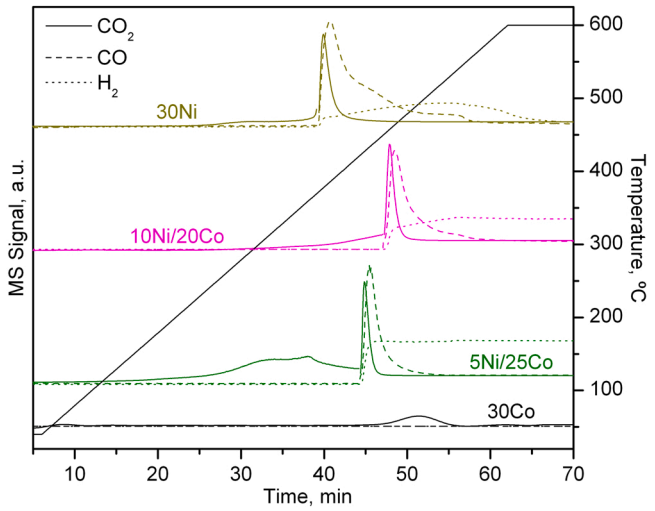

Fig. 7. CH_4-TPRe profiles of the synthesized catalysts.

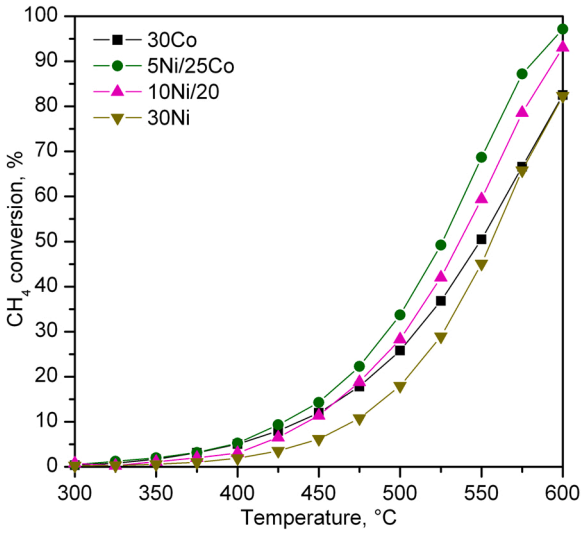

Fig. 8. Light-off curves of methane oxidation over the synthesized catalysts.

be catalyzed by partially reduced or metallic cobalt and/or nickel. Following this rationale, which is schematically depicted in Fig. S4 (Supplementary Material), the most relevant findings derived by this characterization technique were essentially those corresponding to the low temperature range, at which the complete oxidation of methane would be favorably occurring.

The CH_4-TPRe profiles revealed the formation of substantial amounts of CO_2 at two relatively well-discernible temperature windows. On the one hand, the signal detected at lower temperatures (400–450 °C) was attributed to the gradual complete oxidation of methane by oxygen species. Note that no CO or H_2 were detected in this temperature range. On the other hand, when the total oxidation process was no longer possible, the progressive reduction of the catalyst by methane then activated the transformation of the feed into CO, CO_2 and H_2, as can be evidenced by the co-existence of these three products at higher temperatures (500–550 °C). Moreover, the XRD analysis of the spent samples evidenced the presence of metallic cobalt (ICDD 00–015–0806) and nickel (ICDD 00–001–1258), and crystalline coke (ICDD 01–075–1621) (Fig. S5, Supplementary Material).

As aforementioned, only the oxygen species involved in the low-temperature CO_2 formation signal will be assumed to be highly active in the catalytic combustion reaction. After a proper quantification of the amount of formed CO_2, the corresponding amount of consumed oxygen species could be estimated. In this sense, the 5Ni/25Co bimetallic catalyst showed the largest consumption (0.16 mmol O_2 g^{-1}) followed by the 10Ni/20Co sample (0.09 mmol O_2 g^{-1}) and the Co and Ni monometallic catalysts (0.08 and 0.04 mmol O_2 g^{-1}, respectively). In addition, it is worth pointing out that the 5Ni/25Co the oxidation reaction also started at significantly lower temperatures (200 °C) in comparison with the other samples (300–500 °C).

3.2. Catalytic performance

The efficiency in the oxidation of methane into carbon dioxide of the four samples having the same nominal metallic content (30 %wt. %), namely 5Ni/25Co, 10Ni/20Co, 30Co and 30Ni catalysts, was analyzed operating at 300 mL CH_4 g^{-1} h^{-1} between 200 and 600 °C. Three consecutive light-off tests were conducted over each catalyst. After the first test, which could be understood as an equilibration step of the catalyst under reaction conditions, a certain decrease in conversion was observed. Interestingly, no significant differences in conversion were found between the second and third tests resulting in a virtually identical light-off curve. Thus, the conversion profiles shown in Fig. 8 correspond to the third catalytic reaction run. All Co-based samples exhibited 100 % CO_2 selectivity in the whole temperature range. Nevertheless, substantial amounts of carbon monoxide were formed over the 30Ni sample, leading to CO_2 selectivity of only 90 % even at the highest reaction temperatures (600 ºC). It was observed that bimetallic catalysts exhibited a considerably better performance compared with the monometallic samples. The T_{50} values, listed in Table 4, were similar for the two monometallic catalysts (550 °C) and higher than those shown by the bimetallic counterparts (535 °C for 10Ni/20Co and 525 °C for 5Ni/25Co). Table 5.

The specific reaction rates, calculated using the differential method (for conversions less than 20 %) at 450 °C, revealed a higher intrinsic activity of the 5Ni/25Co catalyst (0.80 mmol CH_4 h^{-1} g^{-1}), compared with the monometallic 30Co and 30Ni samples (Table 4). The other investigated bimetallic sample (10Ni/20Co) showed an intermediate behavior (0.63 mmol CH_4 h^{-1} g^{-1}). When referred to the total metallic loading, the best intrinsic activity of the 5Ni/25Co sample was also evidenced. From the correlations depicted in Fig. 9, the observed catalytic activity trend was coherent with the abundance of Co^{3+} species in the samples. Thus, the 5Ni/25Co catalyst presented the highest Co^{3+}/Co^{2+} molar ratio due to the more efficient insertion of Ni^{2+} ions in the structure of the Co_3O_4 spinel leading to the generation of the nickel cobaltite-like species. As shown in Fig. S6 (Supplementary Material), this dependence was also valid when referred to the reaction rate normalized per gram of metal. The excellent behavior of this mixed oxide as oxidation catalyst for a variety of hydrocarbons [44,45], carbon monoxide [46], carbonaceous particulate matter [47] and methane [48] as well has been previously reported. On the other hand, it must be pointed out that both $NiAl_2O_4$ and $CoAl_2O_4$ spinel are not particularly active for the complete oxidation of methane [49,50], owing to their relatively low reducibility and highly stable oxygen species that penalized methane oxidative conversion by the Mars–van Krevelen mechanism. Besides, their formation could be detrimental for the generation of $NiCo_2O_4$ due to the decrease in the amount of available Co_3O_4 and Ni for their mutual interaction. In our study, the formation of this highly active mixed spinel was apparently enhanced with adding small amounts of nickel, since a Ni content as high as 10 %wt. did not lead to a better efficiency than the 30Co catalyst. This was probably owing to the fact that the incorporated Ni was more efficiently dispersed over the 5Ni/25Co catalyst in comparison with the 10Ni/20Co counterpart, as evidenced by its lower NiO/Ni molar ratio. This favored the interaction between Co_3O_4 and the deposited Ni to form $NiCo_2O_4$ to a larger extent as suggested by its large amount of Co^{3+}. This increased presence of easily reducible Co^{3+} was accompanied by a concomitant higher presence of active lattice oxygen species that were able to activate the

Table 4
Redox properties of the synthesized catalysts by H_2-TPR and CH_4-TPRe.

Sample	Low-temperature H_2 uptake, mmol g^{-1}	High-temperature H_2 uptake, mmol g^{-1}	Total H_2 uptake, mmol g^{-1}	Reducibility	Low-temperature O_2 consumption (CH_4-TPRe), mmol g^{-1}
30Co	2.01	3.17	5.18	0.85	0.08
25Co	1.68	2.74	4.42	0.84	—*
5Ni/25Co	1.84	3.29	5.24	0.90	0.16
20Co	1.21	2.16	3.52	0.84	—*
10Ni/20Co	1.52	3.59	5.17	0.92	0.09
30Ni	1.93	2.55	4.48	0.97	0.04

Table 5
Kinetic results of the synthesized catalysts.

Sample	T_{50}, °C	$-r_{CH4}$ at 450 °C, $mmol_{CH4}\ h^{-1}\ g^{-1}$	$-r_{CH4}$ at 450 °C, $mmol_{CH4}\ h^{-1}\ g_{Me}^{-1}$	Apparent activation energy, kJ mol^{-1}
30Co	550	0.67	2.48	90 ± 2
5Ni/25Co	525	0.80	2.96	94 ± 2
10Ni/20Co	535	0.63	2.31	103 ± 2
30Ni	550	0.32	1.18	128 ± 2

oxidation of methane at relatively low temperatures. This was also evidenced by the strong dependence of the intrinsic activity with the O_{latt}/O_{ads} molar ratio and the amount of consumed oxygen at low temperatures in the CH_4-TPRe runs (Fig. 9). On the other hand, it was found that the intrinsic activity of O_{latt} species present in the 30Ni catalyst was significantly lower than that exhibited by the O_{latt} species in the Co-containing catalysts.

The Mars-van Krevelen mechanism, also known as the redox mechanism, has been widely used for kinetics modeling of methane oxidation over metal oxides. This is based on the assumption of a constant oxygen surface concentration on the catalyst, with reaction occurring by interaction between a molecule of reactant and an oxidized portion of the catalyst. Thus, the model assumes that the oxidation of the hydrocarbon occurs in two steps. In the first step, the compound react with the lattice oxygen resulting in its reduction and the corresponding formation of oxygen vacant site. In the second step, the reduced metal oxide is reoxidized by the gas phase oxygen present in the feed. In the steady state, the rates of the reduction and oxidation steps must be equal. Then, the kinetic equation (Eq. 1) can be expressed as:

$$(-r) = \frac{k_{red}k_{ox}P_{CH4}P_{O2}}{k_{ox}P_{O2} + \gamma k_{red}P_{CH4}} \quad (1)$$

where k_{red} is the rate constant of the oxidation of the hydrocarbon by the lattice oxygen, k_{ox} the rate constant of the lattice re-oxidation and γ is the overall stoichiometry of the reaction. For conditions with oxygen excess (in our case, a P_{O2}/P_{CH4} ratio of 10 at the inlet of the reactor), the term $k_{ox}P_{O2}$ is considerably larger than $\gamma k_{red}P_{CH4}$. Consequently, the rate equation simplifies to a power rate law equation (Eq. 2).

$$(-r) \cong k_{red}P_{CH4} \quad (2)$$

Accordingly, the integral method was applied to estimate the apparent activation energy when assuming a first pseudo-order for methane and a zeroth pseudo-order for oxygen [38,51]. Conversions between 10 % and 90 % were fit to the following linearized equation for the integral reactor (Eq. 3) where X is the fractional conversion of methane, k_0 is the pre-exponential factor of the Arrhenius equation and F_{CH40}/W is the weight hourly space velocity. The goodness of the numerical fit is depicted in Fig. S7 (Supplementary Material). It was observed that the apparent activation energy of the 30Ni catalyst (128 kJ mol^{-1}) was markedly higher than that of the cobalt catalysts, in line with the lower activity of this catalyst for complete oxidation. The

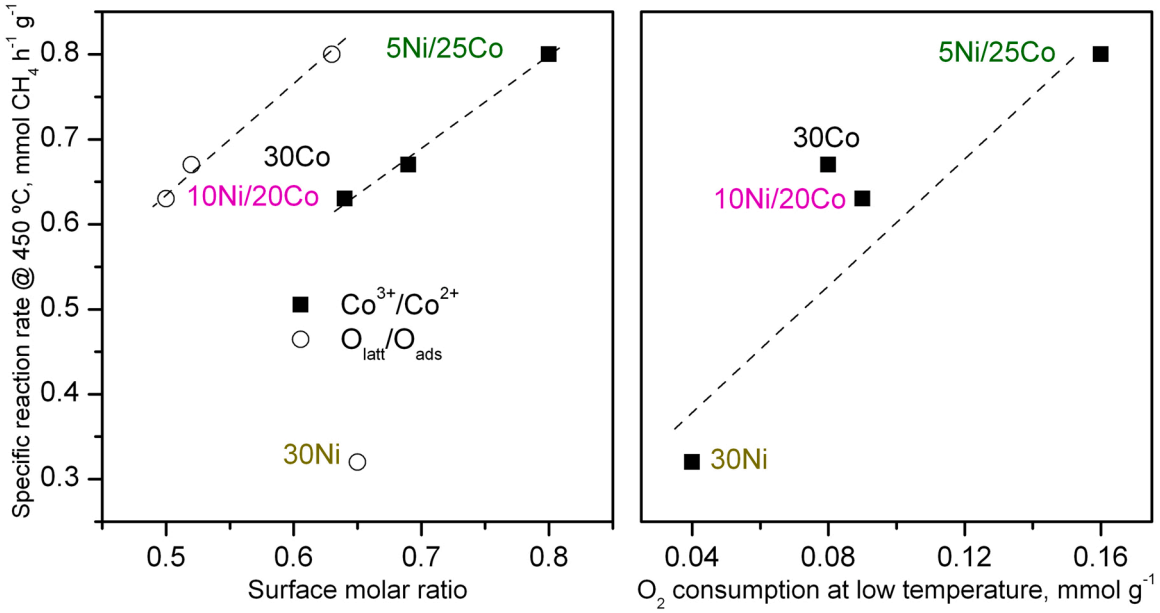

Fig. 9. Relationship among the Co^{3+}/Co^{2+} molar ratio (XPS), O_{latt}/O_{ads} molar ratio (XPS), oxygen consumption at low temperatures (CH_4-TPRe) and the intrinsic activity at 450 °C (reaction runs) of the synthesized catalysts.

bimetallic catalysts and the 30Co catalyst showed a relatively similar value between 90 and 103 kJ mol^{-1}. It is worth pointing out that this range of values was appreciably higher than that found for this reaction catalyzed by bulk Co_3O_4 (70–75 kJ mol^{-1}) [52–54], thereby suggesting that the intrinsic activity of the examined cobalt catalysts was negatively affected by the presence of cobalt aluminate.

$$ln[-ln(1-X)] = ln\left[k_0 C_{CH4_0}\left(\frac{W}{F_{CH4_0}}\right)\right] - \frac{E_a}{RT} \quad (3)$$

Finally, given the presence of notable amounts of water vapor and carbon dioxide in the real exhaust gases of a natural gas engine, an attempt to evaluate the stability of the most efficient catalyst, namely the 5Ni/25Co sample, with time on stream was made. Thus, the evolution of conversion at 575 °C was examined when the composition was alternated following this sequence: 1 %CH_4/10 %O_2/N_2, 1 %CH_4/10 %CO_2 /10 %O_2/N_2, 1 %CH_4/10 %O_2/N_2, 1%CH_4/10 % H_2O 10 %O_2/N_2, 1 %CH_4/10 %O_2/N_2, and 1 %CH_4/10 % H_2O/10 %CO_2/10 %O_2/N_2. For each composition, a reaction time interval of 25 h was analyzed, with an accumulated time on stream of 150 h (Fig. 10). During the first 15–20 h under base conditions (absence of water and CO_2) a slight decrease in conversion from 80 % to 70 % was noticed. Then this conversion was stable, and was not affected by the addition of carbon dioxide for additional 25 h. Therefore, after an initial equilibration of the catalyst under reaction conditions, a relatively good thermal stability and resistance to the presence of CO_2 was evidenced (75 h time on stream). However, after the admission of water into the reactor during additional 25 h, conversion dropped to a stable value of 40 % due to water adsorption on the surface [55]. Interestingly, when water was subsequently cut off, the methane conversion was almost fully recovered (65 %) upon returning to dry conditions. Thus, it was evidenced that this temporary inhibiting effect of water did not result in a remarkable irreversible deactivation of the sample. The catalyst was submitted to a further analysis under humid conditions but combined with the addition of carbon dioxide as well (25 h). Again, a decrease in conversion to 35 % was appreciated due to competitive effects caused by water.

The state of the used catalyst in this long-term run was carried out by N_2 physisorption, XRD and CH_4-TPRe. The textural analysis revealed a slight decrease in surface area to 101 m^2 g^{-1} (107 m^2 g^{-1} for the fresh counterpart), thus suggesting the sintering of the active Co_3O_4 phase as in parallel confirmed by XRD. It is worth highlighting that irreversible poisoning was ruled out in view of the composition of the gas flow at the reactor inlet ($CH_4/O_2/H_2O/CO_2$). Besides, the formation of carbonaceous deposits (coke) was not observed given the net oxidizing character of the feedstream (P_{O2}/P_{CH4}=10 at the inlet of the reactor) that inhibited the eventual decomposition/cracking of methane. Hence, an enlargement of the crystallite size (25 nm, 19 nm for the fresh sample) was verified. These structural changes led in turn to a poorer oxidation ability at low temperatures judging from the results by CH_4-TPRe analysis (Fig. S8, Supplementary Material). A shift of around 10 °C was noted for the peak oxidation temperature, from 410 °C (fresh sample) to 420 °C (used catalyst). However, it must be pointed out that the total amount of active oxygen species was not substantially modified (0.16 mmol O_2 g^{-1}).

4. Conclusions

From a structural point of view, the monometallic samples consisted of a mixture of crystalline Co_3O_4 and amorphous cobalt aluminate in the case of the Co-containing catalysts (20Co, 25Co and 30Co), and a mixture of crystalline NiO and nickel aluminate in the case of the 30Ni sample. The formation of these undesired Al-based spinels due to the unavoidable strong interaction between the transition metal and gamma alumina was appreciable since around 40–65 % of the deposited metal was fixed as a metal-Al mixed oxide. It is worth pointing out that the generation of these aluminates was unfavored with the metallic loading.

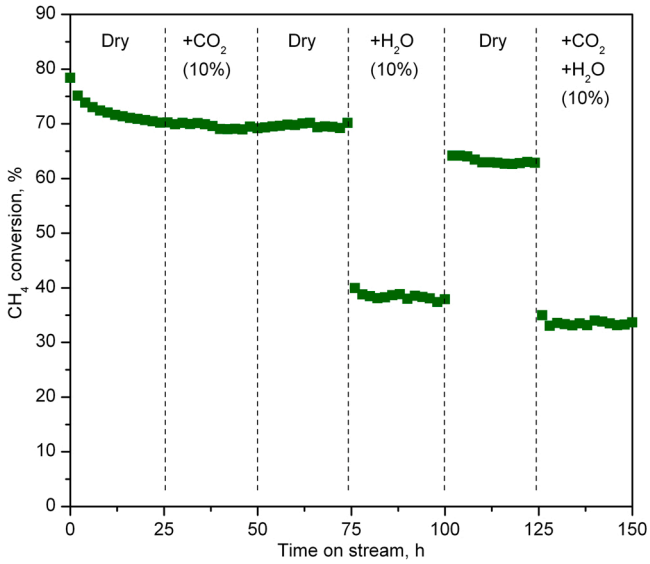

Fig. 10. Evolution of methane conversion with time on stream at 575 °C over the 5Ni/25Co catalyst under varying reaction conditions.

As revealed by STEM-HAADF coupled to chemical mapping the added nickel was homogeneously deposited on the surface of the corresponding cobalt catalyst as no clusters or visible agglomerates were distinguished. Thus, a relative good dispersion of the promoter could be inferred. As a result, the overall redox properties of the bimetallic catalysts were enhanced, which was essentially attributed to the formation of a new $NiCo_2O_4$-like spinel that increased the relative population of Co^{3+} species in the resulting Ni-Co samples. Hence, these structural changes induced by nickel led to an increase in the amount and mobility/reactivity of lattice oxygen species at lower temperatures with respect with the reference pure Co counterparts, which eventually resulted in a higher intrinsic activity and lower ignition temperatures for methane abatement. The optimal catalyst composition, which globally enhanced the abundance of Co^{3+} by a proper combination of highly active Co_3O_4 and $NiCo_2O_4$ phases, was that of the 5Ni/25Co sample. The 10Ni/20Co and the 30Co catalysts exhibited a similar efficiency. Therefore, this study demonstrated that the synergistic effect between the two metal sites is an efficient strategy to activate lattice oxygen species, which can affect the catalytic oxidation activity significantly.

CRediT authorship contribution statement

Andoni Choya: Investigation, Writing - original draft. **Beatriz de Rivas:** Methodology, Formal analysis, Validation. Jose Ignacio **Gutiérrez-Ortiz:** Methodology, Formal analysis, Funding acquisition. **Rubén López-Fonseca:** Conceptualization, Writing - review & editing, Supervision, Funding acquisition, Project administration.

Declaration of Competing Interest

The authors declare that they have no known competing financial interests or personal relationships that could have appeared to influence the work reported in this paper.

Data availability

No data was used for the research described in the article.

Acknowledgments

This research was funded by the Spanish Ministry of Science and Innovation (PID2019-107105RB-I00 AEI/FEDER, UE), Basque

Government (IT1509-22) and the University of The Basque Country UPV/EHU (DOCREC21/23). The authors wish to thank the technical and human support provided by SGIker (UPV/EHU). In addition, authors acknowledge the use of instrumentation as well as the technical advice provided by the National Facility ELECMI ICTS, node 'Advanced Microscopy Laboratory' at University of Zaragoza.

Appendix A. Supporting information

Supplementary data associated with this article can be found in the online version at doi:10.1016/j.jece.2022.108816.

References

[1] K.D. Hajny, O.E. Salmon, J. Rudek, D.R. Lyon, A.A. Stuff, B.H. Stirm, R. Kaeser, C. R. Floerchinger, S. Conley, M.L. Smith, P.B. Shepson, Observations of methane emissions from natural gas-fired power plants, Environ. Sci. Technol. 53 (2019) 8976–8984. ⟨https://pubs.acs.org/doi/10.1021/acs.est.9b01875⟩.

[2] M. Keenan, R. Pickett, E. Tronconi, I. Nova, N. Kinnunen, M. Suvanto, T. Maunula, K. Kallinen, R. Baert, The catalytic challenges of implementing a Euro VI heavy duty emissions control system for a dedicated lean operating natural gas engine, Top. Catal. 62 (2019) 273–281, https://doi.org/10.1007/s11244-018-1127-7.

[3] P. Losch, W. Huang, O. Vozniuk, E.D. Goodman, W. Schmidt, M. Cargnello, Modular Pd/Zeolite composites demonstrating the key role of support hydrophobic/hydrophilic character in methane catalytic combustion, ACS Catal. 9 (2019) 4742–4753.

[4] J. Yang, M. Peng, G. Ren, H. Qi, X. Zhou, J. Xu, F. Deng, Z. Chen, J. Zhang, K. Liu, X. Pan, W. Liu, Y. Su, W. Li, B. Qiao, D. Ma, T. Zhang, A hydrothermally stable irreducible oxide-modified Pd/$MgAl_2O_4$ catalyst for methane combustion, Angew. Chem. Int. Ed. 59 (2020) 1–6.

[5] M. Wu, W. Li, A.T. Ogunbiyi, G. Guo, F. Xue, K. Chen, B. Zhan, Highly active and stable palladium catalysts supported on surface-modified ceria nanowires for lean methane combustion, ChemCatChem 13 (2021) 664–673, https://doi.org/10.1002/cctc.202001438.

[6] Z. Boukha, B. de Rivas, J.R. González-Velasco, J.I. Gutiérrez-Ortiz, Rubén López-Fonseca, Comparative study of the efficiency of different noble metals supported on hydroxyapatite in the catalytic lean methane oxidation under realistic conditions, Materials 14 (2021) 3612, https://doi.org/10.3390/ma14133612.

[7] J. Lin, X. Chen, Y. Zheng, Y. Xiao, Ying Zheng, L. Jiang, Sulfur-resistant methane combustion invoked by surface property regulation on palladium-based catalysts, Appl. Surf. Sci. 587 (2022), 152835, https://doi.org/10.1016/j.apsusc.2022.152835.

[8] M. García-Vázquez, P. Marín, S. Ordóñez, K. Li, J. Tan, G. Zhang, F.R. García-García, Scaling up a hollow fibre reactor: a study on non-PGM hollow fibre after-treatments for methane emission control under extreme conditions, J. Environ. Chem. Eng. 9 (2021), 106880, https://doi.org/10.1016/j.jece.2021.106880.

[9] K. Chen, W. Li, X. Li, A.T. Ogunbiyi, L. Yuan, Irregularly shaped NiO nanostructures for catalytic lean methane combustion, ACS Appl. Nano Mater. 4 (2021) 5404–5412, https://doi.org/10.1021/acsanm.1c00732.

[10] G. Caravaggio, L. Nossova, M.J. Turnbull, Nickel-magnesium mixed oxide catalyst for low temperature methane oxidation, Chem. Eng. J. 405 (2021), 126862, https://doi.org/10.1016/j.cej.2020.126862.

[11] E. Akbari, S.M. Alavi, M. Rezaei, A. Larimi, Catalytic methane combustion on the hydrothermally synthesized MnO_2 nanowire catalysts, Ind. Eng. Chem. Res. 60 (2021) 7572–7587, https://doi.org/10.1021/acs.iecr.1c00881.

[12] A. Palella, L. Spadaro, R. Di Chio, F. Arena, Effective low-temperature catalytic methane oxidation over MnCeOx catalytic compositions, Catal. Today 379 (2021) 240–249, https://doi.org/10.1016/j.cattod.2020.11.010.

[13] S. Fan, W. Zhang, H. Xu, G. Cai, Y. Zhan, X. Chen, Y. Zheng, Tuning lattice defects to facilitate the catalytic performance of Ni–Cu–O hybrid nanoparticles towards methane oxidation, Int. J. Hydrog. Energy 47 (2022) 4536–4545, https://doi.org/10.1016/j.ijhydene.2021.11.060.

[14] R. Suarez Anzorena, M.O. Mazan, A. Soldati, S.A. Larrondo, The effect of incorporation of iron in cerium oxide structure on reducibility and catalytic performance for methane oxidation in diluted streams, Ceram. Int. 45 (2019) 19757–19765, https://doi.org/10.1016/j.ceramint.2019.06.229.

[15] Y. Zheng, Y. Yu, H. Zhou, W. Huang, Z. Pu, Combustion of lean methane over Co_3O_4 catalysts prepared with different cobalt precursors, RSC Adv. 10 (2020) 4490–4498, https://doi.org/10.1039/C9RA09544F.

[16] Q. Yua, C. Liu, X. Li, C. Wang, X. Wang, H. Cao, M. Zhao, G. Wu, W. Su, T. Ma, J. Zhang, H. Bao, J. Wang, B. Ding, M. He, Y. Yamauchie, X.S. Zhao, N-doping activated defective Co_3O_4 as an efficient catalyst for low temperature methane oxidation, Appl. Catal. B: Environ. 269 (2020), 118757, https://doi.org/10.1016/j.apcatb.2020.118757.

[17] S. Yoo, E.W. Lee, D.H. Kim, Methane combustion over mesoporous cobalt oxide catalysts: effects of acid treatment, Mol. Catal. 511 (2021), 111728, https://doi.org/10.1016/j.mcat.2021.111728.

[18] A.H.M. Videla, P. Stelmachowski, G. Ercolino, S. Specchia, Benchmark comparison of Co_3O_4 spinel-structured oxides with different morphologies for oxygen evolution reaction under alkaline conditions, J. Appl. Electrochem. 47 (2017) 295–304, https://doi.org/10.1007/s10800-016-1040-3.

[19] G. Ercolino, P. Stelmachowski, A. Kotarba, S. Specchia, Reactivity of mixed iron–cobalt spinels in the lean methane combustion, Top. Catal. 60 (2017) 1370–1379, https://doi.org/10.1007/s11244-017-0826-9.

[20] Q. Wang, Y. Peng, J. Fu, G.Z. Kyzas, S.M.R. Billah, S. An, Synthesis, characterization, and catalytic evaluation of Co_3O_4/γ-Al_2O_3 as methane combustion catalysts: Significance of Co species and the redox cycle, Appl. Catal. B Environ. 168 (2015) 42–50, https://doi.org/10.1016/j.apcatb.2014.12.016.

[21] A. Choya, B. de Rivas, J.R. González-Velasco, J.I. Gutiérrez-Ortiz, R. López-Fonseca, Oxidation of residual methane from VNG vehicles over Co_3O_4-based catalysts: Comparison among bulk, Al_2O_3-supported and Ce-doped catalysts, Appl. Catal. B Environ. 237 (2018) 844–854, https://doi.org/10.1016/j.apcatb.2018.06.050.

[22] A. Choya, B. de Rivas, J.R. González-Velasco, J.I. Gutiérrez-Ortiz, R. López-Fonseca, On the beneficial effect of MgO promoter on the performance of Co_3O_4/Al_2O_3 catalysts for combustion of dilute methane, Appl. Catal. A Gen. 582 (2019), 117099, https://doi.org/10.1016/j.apcata.2019.05.033.

[23] A. Choya, B. de Rivas, J.I. Gutiérrez-Ortiz, R. López-Fonseca, Comparative study of strategies for enhancing the performance of Co_3O_4/Al_2O_3 catalysts for lean methane combustion, Catalysts 10 (2020) 757, https://doi.org/10.3390/catal10070757.

[24] A. Choya, S. Gudyka, B. de Rivas, J.I. Gutierrez-Ortiz, A. Kotarba, R. López-Fonseca, Design, characterization and evaluation of Ce-modified cobalt catalysts supported on alpha alumina in the abatement of methane emissions from natural gas engines, Appl. Catal. A: Gen. 617 (2021), 118105, https://doi.org/10.1016/j.apcata.2021.118105.

[25] T.H. Lim, S.J. Cho, H.S. Yang, M.H. Engelhard, D.H. Kim, Effect of Co/Ni ratios in cobalt nickel mixed oxide catalysts on methane combustion, Appl. Catal. A: Gen. 505 (2015) 62–69, https://doi.org/10.1016/j.apcata.2015.07.040.

[26] C. Shao, W. Li, Q. Lin, Q. Huang, D. Pi, Low temperature complete combustion of lean methane over cobalt–nickel mixed-oxide catalysts, Energy Technol. 5 (2017) 604–610, https://doi.org/10.1002/ente.201600402.

[27] Y. Dai, V.P. Kumar, C. Zhu, H. Wang, K.J. Smith, M.O. Wolf, M.J. MacLachlan, Bowtie-shaped $NiCo_2O_4$ catalysts for low-temperature methane combustion, Adv. Funct. Mater. 29 (2019), 1807519, https://doi.org/10.1002/adfm.201807519.

[28] J. Chen, X. Zou, Z. Rui, H. Ji, Deactivation mechanism, countermeasures, and enhanced CH_4 oxidation performance of nickel/cobalt oxides, Energy Technol. 8 (2020), 1900641, https://doi.org/10.1002/ente.201900641.

[29] Eurokin. ⟨http://eurokin.org/⟩, 2018 (accessed 21 April 2022).

[30] C. Jiménez-González, Z. Boukha, B. de Rivas, J.J. Delgado, M.A. Cauqui, J. R. González-Velasco, J.I. Gutiérrez-Ortiz, R. López-Fonseca, Structural characterization of Ni/alumina reforming catalysts activated at high temperatures, Appl. Catal. A: Gen. 466 (2013) 9–20, https://doi.org/10.1016/j.apcata.2013.06.017.

[31] Y.J. Wong, M.K. Koh, N.F. Khairudin, S. Ichikawa, Y. Morikawa, A.R. Mohamed, Development of Co supported on Co−Al spinel catalysts from exsolution of amorphous Co−Al oxides for carbon dioxide reforming of methane, ChemCatChem 11 (2019) 5593–5605, https://doi.org/10.1002/cctc.201901098.

[32] X. Zhang, M. Zhao, Z. Song, H. Zhao, W. Liu, J. Zhao, Z. Ma, Y. Xing, The effect of different metal oxides on the catalytic activity of a Co_3O_4 catalyst for toluene combustion: importance of the structure–property relationship and surface active species, N. J. Chem. 43 (2019) 10868–10877, https://doi.org/10.1039/C9NJ01783F.

[33] S. Visweswaran, R. Venkatachalaphy, M. Haris, R. Murugesan, Structural, morphological, optical and magnetic properties of sprayed NiO thin films by perfume atomizer, Appl. Phys. A Mater. 126 (2020) 524, https://doi.org/10.1007/s00339-020-03709-w.

[34] R. Benrabaa, A. Barama, H. Boukhlouf, J. Guerrero-Caballero, A. Rubbens, E. Bordes-Richard, A. Löfberg, R.-N. Vannier, Physico-chemical properties and syngas production via dry reforming of methane over $NiAl_2O_4$ catalyst, Int. J. Hydrog. Energy 42 (2017) 12989–12996, https://doi.org/10.1016/j.ijhydene.2017.04.030.

[35] C. Zhang, Y. Wang, G. Li, L. Chen, Q. Zhang, D. Wang, X. Li, Z. Wang, Tuning smaller Co_3O_4 nanoparticles onto HZSM-5 zeolite via complexing agents for boosting toluene oxidation performance, Appl. Surf. Sci. 532 (2020), 147320, https://doi.org/10.1016/j.apsusc.2020.147320.

[36] Y. Wan, J. Chen, J. Zhan, Y. Ma, Facile synthesis of mesoporous $NiCo_2O_4$ fibers with enhanced photocatalytic performance for the degradation of m ethyl red under visible light irradiation, J. Environ. Chem. Eng. 6 (2018) 6079–6087, https://doi.org/10.1016/j.jece.2018.09.023.

[37] K. Zeng, X. Li, C. Wang, Z. Wang, P. Guo, J. Yu, C. Zhang, X.S. Zhao, Three-dimensionally macroporous MnZrOx catalysts for propane combustion: Synergistic structure and doping effects on physicochemical and catalytic properties, J. Colloid Interf. Sci. 572 (2020) 281–296, https://doi.org/10.1016/j.jcis.2020.03.093.

[38] F. Zasada, J. Janas, W. Piskorz, M. Gorczyńska, Z. Sojka, Total oxidation of lean methane over cobalt spinel nanocubes controlled by the self-adjusted redox state of the catalyst: experimental and theoretical account for interplay between the Langmuir–Hinshelwood and Mars–Van Krevelen mechanisms, ACS Catal. 7 (2017) 2853–2867, https://doi.org/10.1021/acscatal.6b03139.

[39] J. González-Prior, R. López-Fonseca, J.I. Gutiérrez-Ortiz, B. de Rivas, Catalytic removal of chlorinated compounds over ordered mesoporous cobalt oxides synthesized by hard-templating, Appl. Catal. B: Environ. 222 (2018) 9–17, https://doi.org/10.1016/j.apcatb.2017.09.050.

[40] Y. Wang, C. Wang, M. Chen, J. Hu, Z. Tang, D. Liang, W. Cheng, Z. Yang, J. Wang, H. Zhang, Influence of $CoAl_2O_4$ spinel and Co-phyllosilicate structures derived from Co/sepiolite catalysts on steam reforming of bio-oil for hydrogen production, Fuel 279 (2020), 118449, https://doi.org/10.1016/j.fuel.2020.118449.

[41] R. López-Fonseca, C. Jiménez-González, B. de Rivas, J.I. Gutiérrez-Ortiz, Partial oxidation of methane to syngas on bulk $NiAl_2O_4$ catalyst. Comparison with alumina supported nickel, platinum and rhodium catalysts, Appl. Catal. A: Gen. 437–438 (2012) 53–62, https://doi.org/10.1016/j.apcata.2012.06.014.

[42] J.L. Ewbank, L. Kovarik, F.Z. Diallo, C. Sievers, Effect of metal–support interactions in Ni/Al_2O_3 catalysts with low metal loading for methane dry reforming, Appl. Catal. A: Gen. 494 (2015) 57–67, https://doi.org/10.1016/j.apcata.2015.01.029.

[43] J. Zhou, H. Ma, C. Liu, H. Zhang, W. Qian, W. Ying, Ni based catalysts supported on Ce modified MgAl spinel supports for high temperature syngas methanation, Catal. Lett. 149 (2019) 2563–2574, https://doi.org/10.1007/s10562-019-02868-7.

[44] Y. Huang, W. Fan, B. Long, H. Li, W. Qiu, F. Zhao, Y. Tong, H. Ji, Alkali-modified non-precious metal 3D-$NiCo_2O_4$ nanosheets for efficient formaldehyde oxidation at low temperature, J. Mater. Chem. A 4 (2016) 3648–3654, https://doi.org/10.1039/C5TA09370H.

[45] K. Li, T. Li, Y. Dai, Y. Quan, J. Zhao, J. Ren, Highly active urchin-like MCo_2O_4 (M = Co, Cu, Ni or Zn) spinel for toluene catalytic combustion, Fuel 318 (2022), 123648, https://doi.org/10.1016/j.fuel.2022.123648.

[46] N. Neha, R. Prasad, S.V. Singh, Simultaneous catalytic oxidation of a lean mixture of CO-CH_4 over spinel type cobalt based oxides, Bull. Chem. React. Eng. Catal. 15 (2020) 490–500, https://doi.org/10.9767/bcrec.15.2.6499.490-500.

[47] M. Zhao, J. Deng, J. Liu, Y. Li, J. Liu, Z. Duan, J. Xiong, Z. Zhao, Y. Wei, W. Song, Y. Sun, Roles of surface-active oxygen species on 3DOM cobalt-based spinel catalysts $M_xCo_{3-x}O_4$ (M = Zn and Ni) for NOx-assisted soot oxidation, ACS Catal. 9 (2019) 7548–7567, https://doi.org/10.1021/acscatal.9b01995.

[48] Q. Huang, W. Li, Q. Lin, X. Zheng, H. Pan, D. Pi, C. Shao, C. Hu, H. Zhang, Catalytic performance of Pd-$NiCo_2O_4/SiO_2$ in lean methane combustion at low temperature, J. Energy Inst. 91 (2018) 733–742, https://doi.org/10.1016/j.joei.2017.05.008.

[49] X. Zou, J. Chen, Z. Rui, H. Ji, Sequential growth reveals multi-spinel interface promotion for methane combustion over alumina supported palladium catalyst, Appl. Catal. B: Environ. 273 (2020), 119071, https://doi.org/10.1016/j.apcatb.2020.119071.

[50] X. Zou, Z. Rui, S. Song, H. Ji, Enhanced methane combustion performance over $NiAl_2O_4$-interface-promoted Pd/γ-Al_2O_3, J. Catal. 338 (2016) 192–201, https://doi.org/10.1016/j.jcat.2015.12.031.

[51] E. Genty, S. Siffert, R. Cousin, Investigation of reaction mechanism and kinetic modelling for the toluene total oxidation in presence of CoAlCe catalyst, Catal. Today 333 (2019) 28–35, https://doi.org/10.1016/j.cattod.2018.03.018.

[52] J. Li, X. Liang, S. Xu, J. Hao, Catalytic performance of manganese cobalt oxides on methane combustion at low temperature, Appl. Catal. B Environ. 90 (2009) 307–312, https://doi.org/10.1016/j.apcatb.2009.03.027.

[53] S. Nasr, R.E. Hayes, N. Semagina, Stability of kinetic parameters of Co_3O_4/CeO_2 catalyzed methane combustion, Can. J. Chem. Eng. 99 (2021) 2670–2676, https://doi.org/10.1002/cjce.24054.

[54] A. Choya, B. de Rivas, J.I. Gutiérrez-Ortiz, R. López-Fonseca, Bulk Co_3O_4 for methane oxidation: effect of the synthesis route on physico-chemical properties and catalytic performance, Catalysts 12 (2022) 87, https://doi.org/10.3390/catal12010087.

[55] B.C. Enger, Å.L. Fossan, Ø. Borg, E. Rytter, A. Holmen, Modified alumina as catalyst support for cobalt in the Fischer–Tropsch synthesis, J. Catal. 284 (2011) 9–22, https://doi.org/10.1016/j.jcat.2011.08.008.